O_3-precursor relationship over multiple patterns of time scale: A case study in Zibo, Shandong Province, China

Zhensen Zheng[1], Kangwei Li[2,3*], Bo Xu[4], Jianping Dou[5], Liming Li[1], Guotao Zhang[1], Shijie Li[1], Chunmei Geng[1], Wen Yang[1], Merched Azzi[6], Zhipeng Bai[1*]

[1] State Key Laboratory of Environmental Criteria and Risk Assessment, Chinese Research Academy of Environmental Sciences, Beijing 100012, China
[2] Univ Lyon, Université Claude Bernard Lyon 1, CNRS, IRCELYON, F-69626 Villeurbanne, France
[3] Department of Environmental Sciences, University of Basel, 4056, Basel, Switzerland
[4] Zibo Eco-Environmental Monitoring Center, Zibo 255000, China
[5] Zibo Ecological Environment Quality Control Service Center, Zibo 255095, China
[6] New South Wales Department of Planning, Industry and Environment, PO Box 29, Lidcombe, NSW 1825, Australia

***Corresponding authors**:
Kangwei Li (likangweizju@foxmail.com, kangwei.li@unibas.ch) and Zhipeng Bai (baizp@craes.org.cn)

Abstract. In this study, we developed an approach that integrated multiple patterns of time scale for box modeling (MCMv3.3.1) to better understand the O_3-precursor relationship through multiple sites and continuous observations. A five-month field campaign was conducted in the summer of 2019 to investigate the ozone formation chemistry at three sites in a major prefecture-level city (Zibo) in Shandong province of northern China. It was found that the relative incremental reactivity (RIR) of major precursor groups (e.g., anthropogenic volatile organic compound (AVOC), NO_x) was overall consistent in the sign along with time scales changed from wider to narrower (four patterns: five-month, monthly, weekly, and daily) at each site, though the magnitudes of RIR varied at different sites. The time series of the photochemical regime (using RIR_{NOx}/RIR_{AVOC} as indicator) in weekly or daily patterns further showed a synchronous temporal trend among the three sites, while the magnitude of RIR_{NOx}/RIR_{AVOC} was site-to-site dependent. The derived RIR ranking (top 10) of individual AVOC species showed consistency at three patterns (i.e., five-month, monthly, and weekly). It was further found that the campaign-averaging photochemical regimes showed overall consistency in the sign but non-negligible variability among

the four patterns of time scale, which was mainly due to the embedded uncertainty in model input dataset when averaging individual daily pattern into different timescales. This implies that utilizing narrower time scale (i.e., daily pattern) is useful to derive reliable and robust O_3-precursor relationship. Our results highlight the importance of quantifying the impact of different time scales to constrain the photochemical regime, which can formulate more accurate policy-relevant guidance for O_3 pollution control.

1 Introduction

Since 2013, the ambient $PM_{2.5}$ concentration in China has dramatically declined by implementing Clean Air Action (Lu et al., 2018; Wang et al., 2020b; Zhang et al., 2019). However, national ground surface ozone concentrations increased over the same period (Xue et al., 2020) and became a major air quality problem that needed to be addressed in China (Li et al., 2019; Wang et al., 2019). It is well-known that ground surface ozone is formed mainly by complex nonlinear photochemical oxidation of volatile organic compounds (VOCs) in the presence of nitrogen oxides (NO_x = NO + NO_2) and sunlight (Blanchard, 2000; Hidy, 2000; Kleinman, 2000), which adversely influences human health, vegetation and corps (Brunekreef and Holgate, 2002; Vingarzan, 2004).

Given the complex non-linear relationship between O_3 formation and its precursors (VOCs and NO_x), challenges in mitigating its severity lie primarily in comprehensively understanding of O_3-precursor relationship (Su et al., 2018a; Tan et al., 2018a). It is commonly recognized that regional-scale air quality models and the 0-D box model are two mainstream approaches to investigate the increasingly severe ozone problem (Blanchard, 2000; Cardelino and Chameides, 1995; Hidy, 2000; Liu et al., 2019). Unlike the complicated 3-D air quality models, the 0-D box model is an observation-based model that implemented with gas-phase chemical mechanism, and has been widely used to diagnose O_3-precursor relationship in various locations (Liu et al., 2021a; Sun et al., 2016; Tan et al., 2019b; Xue et al., 2014a; Yu et al., 2020a). Some previous studies (Li et al., 2021; Lu et al., 2010a; Sicard et al., 2020; Yu et al., 2020b) have reported a large variability of O_3-precursor relationship in spatiotemporal scales in many cities of China, which indicates great challenges in current O_3 pollution control (Wang et al., 2017a; Xue et al., 2014b).

Table 1 summarizes the published studies of O_3-precursor relationship using the 0-D box model (implemented with different gas-phase chemical mechanisms) at diversified patterns of time scale in many places of China. The observational period in most previous studies was short-term (i.e., less than one month), while medium-term (i.e., from one to several months), and long-term (i.e., multiple years) periods were limited. As shown in **Table 1**, we find that model input datasets with different

timescales have been employed in previous studies to identify the campaign-averaging O_3 formation regime, but there is a lack of comparison among these different timescales. We also find that more than half of the studies using the averaged diurnal patterns as box model input, which is particularly common for those medium and long-term measurements. For example, a 10 years long-term observational study by Wang et al., (2017a) adopted monthly pattern of time scale for model simulation with the reason of saving computing resources, and it also revealed a substantial temporal variability of O_3-precursor relationship. In addition, it is believed that long-term (measurements of at least several months) and multiple-site continuous online measurements can provide opportunity to develop O_3 control strategy more comprehensively over a wider spatiotemporal scale (Li et al., 2021; Wang et al., 2017b; Wang et al., 2017b). However, such measurements have been quite rare in China, limiting the present understanding of O_3-precursor relationship (Lu et al., 2019; Wang et al., 2017b).

In this study, a five-month field campaign was conducted in the summer of 2019 to investigate the ozone formation chemistry at 3 sites in Zibo, a major prefecture-level Chinese city in Shandong province. According to our measurements at the three sites in Zibo, the averaged O_3 concentration during the whole observational period was around 50 ppbv, while the daily maximum of O_3 concentrations for some extremely polluted periods were nearly 120-150 ppbv (see details in **Section 3.1**). Here we developed an approach that integrated multiple patterns of time scale for box model simulation, which aimed at illustrating the non-linearity of O_3-precursor relationship driven by its actual daily / weekly / monthly variability. Our results can be conducive to interpreting variations of O_3-precursor relationship over a wider spatiotemporal scale, and they provide implications for developing more precise and constrained O_3 control strategies in other regions.

2 Methods

2.1 Study sites and measurements

Field measurements were conducted in a major prefecture-level city (Zibo), which is in the middle of Shandong Province, northern China, from 1 May to 30 September, 2019. **Figure S1** shows the surrounding environment and geographical locations at the three sampling sites; a detailed description of the Tianzhen (TZ), Beijiao (BJ) and Xindian (XD) sites can be found in our previous study (Li et al., 2021). Briefly, TZ contains a mixture of crude oil processing and operation stations and farming areas, and is classified as suburban area; XD contains a mixture of residential and heavy industrial zones, and is considered as a suburban area; BJ is in the urban area of Zibo.

Typical inorganic gases of O_3, NO, NO_2, CO and SO_2 were measured using online commercial gas analysers (Thermo Scientific 49i, 42i, 48i and 43i, USA) at the three sites. Following the Chinese meteorological monitoring regulation (GB/T 35221-2017),

we continuously monitored the meteorological parameters (i.e., temperature, relative humidity, UV-A solar radiation, precipitation, wind speed, and wind direction) at the three sites (Li et al., 2021). Two online GC systems (gas chromatography–flame ionisation detector, GC-FID, Thermo Scientific GC5900) were deployed at TZ and BJ respectively to measure VOC species. For C_2-C_5 VOCs, desorption and separation were performed using a GC with pre-concentration on a combination of two columns, followed by a FID detector. For C_6-C_{12} VOCs, air sample was pre-concentrated on Tenax GR cartridges and subsequently separated by chromatographic column, then detected by another FID detector. Similarly, one online system (gas chromatography–flame ionisation detector/photoionisation detector, GC-FID/PID, Syntech Spectras GC 955-615/815) was deployed at XD site. For C_2-C_6 VOCs, the hydrocarbons were concentrated on a Tenax GR carrier, then thermally desorbed and separated on a DB-1 column, and finally detected by FID and PID detectors. For C_6-C_{12} VOCs, the air sample was concentrated on a Carbosieves SIII carrier at 5°C, then thermally desorbed and separated on a combination of two columns, and FID and PID detectors were employed for subsequent detection. These systems measured 55 VOC species at a 1-h resolution, and more detailed descriptions can be found elsewhere (Chien, 2007; Jiang et al., 2018; Xie et al., 2008).

Table S1 summarized the limit of detection, accuracy, precision of the instruments at the three sites, and all the measurement instruments were regularly subjected to the service of checking and maintenance during the whole campaign. Unfortunately, we did not conduct the inter-comparison between the GC-FID and GC-FID/PID instruments at the same site due to practical reasons, as these VOC instruments were separately deployed at the three different sites for continuous routine operation. To ensure the quality assurance / quantity control (QA/QC) of online VOC measurement, two five-point calibrations (i.e., 2, 4, 6, 8, 10 ppbv, dilution from one cylinder) for standard gases with 55 VOC species (Linde Co., Ltd, USA) were carried out in May and August of 2019 at the three sites. **Table S2** showed that the calibration linearity (R^2) of all measured VOCs were nearly 0.9990. Additionally, a single-point calibration (i.e., 6 ppbv) was regularly performed every month during the whole campaign. As shown in **Figure S2** (a case from TZ), the retention time, peak fitting and baseline of the chromatogram were manually checked and adjusted on a daily basis.

2.2 0-D box model and design of four patterns of time scale

The 0-D box model integrated with the latest Master Chemical Mechanism of MCMv3.3.1 (http://mcm.york.ac.uk/) has been widely utilized in many regions (He et al., 2019; Jenkin et al., 2015; Liu et al., 2019; Whalley et al., 2021). Unlike the lumped chemical mechanisms such as CB05 (Wang et al., 2017a; Yarwood et al., 2005), CB6 (Yarwood et al., 2010), RACM/RACM2 (Goliff et al., 2013; Stockwell et al., 1997,

2020) and SAPRC-07 (Carter, 2010), the MCMv3.3.1 is a near-explicit chemical mechanism consisting of over 5,800 species and 17,000 reactions (Jenkin et al., 2015; Saunders et al., 2003), which can be used to describe the gas-phase chemistry (i.e., in-situ photochemistry). In this study, the box model (based on the Framework for 0-D Atmospheric Modeling, F0AM) (Wolfe et al., 2016) was applied and constrained by the mean diurnal profiles of meteorological data (i.e., temperature, relative humidity, and photolysis rates), 4 inorganic gases (i.e., SO_2, CO, NO, and NO_2), and 45 speciated VOCs (in MCMv3.3.1 species list; see **Table S3**). Since measured photolysis rates (*J* values) were not available, the measured UV-A solar radiation was used to scale the photolysis rates calculated from the Tropospheric Ultraviolet and Visible Radiation model (TUVv5.2; https://www.acom.ucar.edu/Models/TUV/Interactive_TUV/) following the approach of recent studies (Lyu et al., 2019; Lyu et al., 2016). Specifically, the geographical coordinates, date and time were initialized into the TUV model to derive photolysis rates and solar radiation. We obtained the scaling factor by comparing the observed with modeled solar radiation, and used this scaling factor to scale the TUV model derived photolysis rates. A dilution rate of 3/86400 s^{-1} was applied for all non-constraint species and simulation days through a stepwise sensitivity test by adjusting it from 1/86400 s^{-1} to 5/86400 s^{-1} (see details in **Text S1**) for the best reproduction of O_3. For each model run (i.e., each daily model simulation), it was performed on a daily basis with intervals of 24 hours spanning from 0:00 to 23:00, and each individual model simulation was run to reach one-day diurnal steady state. The detailed descriptions of box model operation were provided in our previous study (Li et al., 2021).

Since the box model simulations are conducted with intervals of 24 hours spanning from 0:00 to 23:00 local standard time (Wang et al., 2018), the entire campaign observations were taken into four patterns of time scale (i.e., five-month, monthly, weekly, and daily) as diurnal average format for model input (**Figure 1**). Note that some days or weeks were not modeled due to some missing data in the measurements. Nevertheless, the total simulation number at the daily (i.e., 100, 81, and 114 days for TZ, BJ and XD respectively) or weekly (i.e., 21, 20, and 19 weeks for TZ, BJ, and XD respectively) scale was representative of the five-month campaign. Specifically, the entire campaign data classified as four patterns of time scale were modeled as base runs. Then we performed the sensitivity modeling to calculate the relative incremental reactivity (RIR) of precursors by adjusting the input concentrations in the base runs (see next section) (Lu et al., 2010a).

2.3 Calculation of net O_x production rate $P(O_x)$ and Relative incremental reactivity (RIR)

Considering the rapid chemical titration of NO to NO_2 in the presence of O_3, the concept of 'total oxidant' ($O_x = O_3 + NO_2$) has been widely used to represent the actual

photochemical production of O_3 (Lu et al., 2010). Similar to those described in previous studies using the 0-D box model (He et al., 2019; Lyu et al., 2016), the net or in-situ O_x production rate ($P(O_x)$) is defined as the difference between the O_x gross production rate ($G(O_x)$) and the O_x destruction rate ($D(O_x)$), which is formulated in accordance with Eq. (1):

$$P(O_x) = G(O_x) - D(O_x) \quad (1)$$

The O_x gross production rate ($G(O_x)$), or the total chemical production of O_x, is calculated by summing the rates of oxidation of NO by HO_2 and RO_2 radicals in accordance with Eq. (2):

$$G(O_x) = k_{HO_2+NO}[HO_2][NO] + \sum k_{RO_{2,i}+NO}[RO_{2,i}][NO] \quad (2)$$

The O_x destruction rate ($D(O_x)$), or total chemical loss of O_x, is calculated by summing O_3 photolysis, the reaction of O_3 with OH, HO_2 and alkenes, as well as the reaction between NO_2 and OH, as described by Eq. (3):

$$D(O_x) = k_{O^1D+H_2O}[O^1D][H_2O] + k_{OH+O_3}[OH][O_3] + k_{HO_2+O_3}[HO_2][O_3] + k_{alkenes+O_3}[alkenes][O_3] + k_{OH+NO_2}[OH][NO_2] \quad (3)$$

Concentrations of radicals and intermediates are obtained from the outputs of the 0-D box model. The k values in Eq. (2) and (3) represent the rate constants of the corresponding reactions, respectively. The subscript 'i' in Eq. (2) represents the individual RO_2 species.

Additionally, relative incremental reactivity (RIR) has been widely used as a metric to quantify the O_3-precursor relationship, and it can be derived from the 0-D box model (MCMv3.3.1) by changing the input mixing ratios of its precursors (Sillman, 2010; Xue et al., 2014a). The RIR is defined as the ratio of percentage change in net O_x (O_x = O_3 + NO_2) production rate $P(O_x)$ (Li et al., 2021) to percentage change of concentration of precursor X. The RIR of a specific precursor X is described in Eq. (4):

$$RIR(X) = \frac{[PO_x(CX) - PO_x(CX - \Delta CX)]/PO_x(CX)}{\Delta CX/CX} \quad (4)$$

Here, X is a specific precursor (i.e., NO_x, CO or grouped / individual VOC species), CX is the measured concentration of precursor X, and ΔCX is the hypothetical concentration change (ΔCX/CX = 10% in this study in accordance with the previous studies (Lyu et al., 2016; Wang et al., 2018)). $PO_x(CX)$ represents the simulated O_x production rate in a base run, whereas $PO_x(CX–\Delta CX)$ is the simulated O_x production in a second run with a hypothetical concentration change of species X. Obviously, a higher positive value of RIR(X) suggests a more effective way of reducing the ambient O_3 production rate by reducing X (Ling et al., 2011; Zhang et al., 2008a).

In this study, the O_3 precursors were divided into four major categories, including anthropogenic VOC (AVOC), biogenic VOC (BVOC, only isoprene in this study), CO and NO_x (Tan et al., 2019b). AVOC was further divided into three subcategories: alkanes,

aromatics and alkenes* (the asterisk denotes anthropogenic alkenes, excluding isoprene in this study) (Yu et al., 2020a). As mentioned, RIR method was applied mainly to evaluate the O_3-NO_x-VOC sensitivity and determine the photochemical regimes among four patterns of time scale. Thus, we calculated the RIR values of major precursor groups (i.e., AVOC, BVOC, CO, NO_x, alkanes, alkenes* and aromatics) to further quantify the O_3-precursor relationship.

In general, O_3 formation chemistry is usually classified into three regimes (i.e., VOC-limited, transitional and NO_x-limited) (He et al., 2019; Wang et al., 2018). In this study, RIR_{NOx}/RIR_{AVOC} (the ratio of two RIR values) was used as a metric to classify the photochemical regimes (Li et al., 2021). Specifically, RIR_{NOx}/RIR_{AVOC} value of less than 0.5 was defined as VOC-limited regime, greater than 2 as NO_x-limited regime, and from 0.5 to 2 as transitional regime (see **Text S2** and **Table S4**) (Li et al., 2021).

3 Results and discussion

3.1 Overview of the field campaign

Figure 2 shows the time series of measured meteorological parameters and O_3 as well as its precursors at the three sites during the whole campaign. In general, the temperature (*T*) and relative humidity (RH) were basically consistent at the three sites, while the wind speeds were different, which suggests that the three sites had an overall consistent meteorological condition. In addition, the time series of UV-A radiation was shown in **Figure 2d**, which was only available from one urban site of Zibo but expected to represent the whole Zibo city in this study. Following the protocol of the previous studies (Lyu et al., 2019; Wang et al., 2017b; Xue et al., 2014), the time series of photolysis rates (e.g., J_{NO_2} (**Figure 2e**) and J_{O^1D} (**Figure 2f**)) were calculated from TUVv5.2 model and further scaled from UV-A radiation measurement.

As shown in **Figure 2g**, we found that severe O_3 pollution was observed at the three sites throughout the whole campaign. According to our measurements at the three sites in Zibo, the averaged O_3 concentration during the whole observational period was around 50 ppbv, while the daily maximum of O_3 concentrations for some extremely polluted periods were nearly 120-150 ppbv (**Figure 2g**). Interestingly, the O_3 concentrations at the three sites were generally consistent, while the levels of its precursors (e.g., VOC, NO_x) were obviously different (**Figure 2h-k**), which implies the site-to-site variation of O_3 formation chemistry for the whole Zibo city.

Generally, OH reactivity (or OH loss rate, k_{OH}) is widely applied to quantify the capacity of OH consumption by VOCs (Tan et al., 2019a). According to **Table S3**, the BVOC reactivity (k_{BVOC}, 3.5 ± 4.1 s^{-1}) in TZ were highest among the three sites. As BJ was mainly influenced by the emission from urban region, it showed the highest AVOC reactivity (k_{AVOC}, 6.8 ± 6.3 s^{-1}) and NO_x level (31.1 ± 28.6 ppbv). In addition, XD showed the highest level of alkenes* reactivity of 4.0 ± 3.2 s^{-1} within the three sites,

and the local petrochemical industry nearby XD area may explain such characteristic (Li et al., 2021).

3.2 Evaluation of box model performance

The measured O_3 concentrations were not constrained in our MCMv3.3.1 box model calculation, thus the model performance could be quantitatively assessed by comparing the modeled O_3 (from base runs) with the measured O_3. **Figure S3-S8** show the time series of simulated and observed O_3 concentrations at four patterns of time scale. In most cases, the box model simulation could accurately capture the level and variation trend of the observed O_3. However, on some days the modeling results underestimated or overestimated the O_3 concentrations, particularly the underestimation of nocturnal O_3 concentrations. Such discrepancies between the simulated and observed O_3 were likely due to limitations in explicit representations of atmospheric and transport processes (i.e., the horizontal and vertical transport process of ground ozone) by 0-D modeling approach (Lyu et al., 2019; Yu et al., 2020b). Specifically, ozone simulated by the 0-D box model is considered as in-situ photochemical processes from its precursors. Unlike the 3-D air quality model, 0-D box model usually simplifies the representation of the physical processes (i.e., deposition and advection) (Lu et al., 2010a; Sillman, 2010). Note that some adjustable parameters (e.g., radiation scheme, dilution rate) were remained consistent in all of our model calculations, which ensured the comparability of model results to the greatest extent.

The index of agreement (*IOA*) (Li et al., 2021; Lyu et al., 2016), Pearson's correlation coefficient (*r*) and root mean square error (*RMSE*) were jointly used as statistical metrics to quantify the goodness-of-fit between the simulated and observed O_3 concentrations. **Table S5** summarizes these statistical metrics for each site at various patterns of time scale. Because any single statistical metric has its own limitations, using these three indicators conjointly provided a more comprehensive evaluation of the model performance (Su et al., 2018b). Generally, higher *IOA* and *r* as well as lower *RMSE* indicate better agreement between the simulated and observed values (Wang et al., 2018; Willmott, 1982). As shown in **Table S5**, slightly reduced correlation was observed as the time scale changed from the wider (i.e., five-month scale) to the narrower (i.e., daily scale) pattern, which is understandable because of the enlarged statistical samples in the narrower pattern of time scale.

In summary, TZ showed the best performance of the box model simulation, followed by XD and BJ, regardless of any statistical metrics or different patterns of time scale, which may be associated with the optimized dilution rate for non-constraint species in model configuration. The overall model performance in this study (i.e., a day-to-day *IOA* of approximately 0.90 for TZ) was close to or slightly better than those reported in previous studies, such as *IOA* = 0.74 in Hong Kong (Liu et al., 2019), *IOA*

= 0.74 in Wuhan (Lyu et al., 2016) and *IOA* = 0.90 in Jiangmen (He et al., 2019). According to the above evaluation of base runs, our modeled results were acceptable for the subsequent O_3-precursor relationship analysis described in the following sections.

3.3 Month-to-month

Figure 3a-b presents the monthly RIR values of the major precursor groups at each site, and the large variability of O_3-precursor relationship at spatiotemporal scale (i.e., site-to-site and month-to-month) was observed. Specifically, in most months, XD generally showed the highest RIR_{AVOC} among the three sites, followed by BJ and TZ. In addition, RIR_{BVOC} showed similar level to RIR_{AVOC} in TZ, but much less than RIR_{AVOC} in BJ and XD, which can be explained by the observed higher BVOC reactivity in TZ than the other two sites (see **Figure S9** and **Table S3**). Also, almost all the precursor groups showed positive RIR values, except negative RIR_{NO_x} appeared in BJ and XD in September. In addition, the RIR_{CO} values at the three sites suggested its limited role in O_3 formation at the three sites, compared with other major categories of O_3 precursors. Among the three subcategories of AVOC, alkenes* always had the highest RIR values, followed by aromatics, while the contribution of alkanes to O_3 formation can be ignored due to their near-zero RIR values. That sequence of O_3-AVOC sensitivity (alkenes* > aromatics > alkanes) indicated by the RIR analysis was consistent with previous studies in some other Chinese cities (Su et al., 2018b; Tan et al., 2019b). Significant monthly variations of O_3, NO_x, CO, VOC reactivity and TVOC/NO_x ratios (in ppbC/ppbv, as a widely used simple metric to determine the photochemical regime) (National Research Council, 1991) were also observed from May to September (see **Figure S9** and **Table S3**) at the three sites. For example, the BVOC reactivity in TZ showed highest level among the three sites during the whole campaign, and the AVOC reactivity in BJ showed more considerable variations in different months, which indicated spatial and temporal variations of local primary emission for O_3 precursors in Zibo city.

Figure 3c shows monthly RIR_{NOx}/RIR_{AVOC} at each site, which clearly reveals the spatial and temporal variations in photochemical regimes. For instance, the photochemical regime at the TZ site was considered to be transitional regime in May, NO_x-limited regime in June and July, and VOC-limited regime in August and September; whereas for a specific month like June, NO_x-limited, VOC-limited, and transitional regimes were generally identified for TZ, BJ, and XD respectively. **Figure 5b** shows good consistency between monthly TVOC/NO_x and RIR_{NOx}/RIR_{AVOC}, suggesting that the changes of local emissions for O_3 precursors may partially explain the considerable variation of O_3 formation chemistry in different months.

3.4 Week-to-week

Figure 4 shows the time series of week-to-week RIR values of major precursor groups and RIR_{NOx}/RIR_{AVOC} at three sites in Zibo. Compared with month-to-month results, **Figure 4** further reveals the O_3-precursor relationship with more information in temporal trends. The temporal variations in weekly RIR_{AVOC} at the three sites generally decreased and then increased, whereas weekly RIR_{NOx} represented an opposite temporal variation during the entire campaign. Additionally, weekly RIR_{BVOC} showed a trend of first decrease and then increase at TZ, while it did not show clear temporal variation at BJ and XD due to low values (**Figure 4a-c**). In general, $RIR_{alkanes}$, $RIR_{alkenes*}$ and $RIR_{aromatics}$ showed a tendency consistent with that of the RIR_{AVOC} at three sites (**Figure 4d-f**). Overall, these phenomena were consistent among the three sites, though the magnitude of RIR values varied site-to-site. In parallel, the temporal changing of O_3 precursor (e.g., AVOC, NO_x) was also observed at the three sites during the entire campaign (see **Figure S10**). For example, the weekly NO_x concentration showed an overall trend of first decrease and then increase, while the AVOC reactivity showed a different temporal variation. Given the moderate correlation between weekly $TVOC/NO_x$ and RIR_{AVOC}/RIR_{NOx} (**Figure 5c**), the temporal variations of RIR values and O_3 formation chemistry at the three sites may be partially elucidated by the emission changes of O_3 precursors.

As shown in **Figure 4g-i**, all the three sites showed similar temporal trends of RIR_{NOx}/RIR_{AVOC}, as it increased first and then decreased, though the magnitude of RIR_{NOx}/RIR_{AVOC} varied largely at each site. Such site-to-site variability of RIR_{NOx}/RIR_{AVOC} suggests that the photochemical regime in a local scale was mainly influenced by local emissions. By contrast, the site-to-site synchronization in temporal trend of RIR_{NOx}/RIR_{AVOC} suggests that the photochemical regime in a local scale may also be influenced by the emissions in a regional area. Therefore, the long-term, week-to-week RIR_{NOx}/RIR_{AVOC} of multiple sites can further reflect the variability of ozone formation regime at a large geographic scale.

3.5 Day-to-day

In this section, O_3-precursor relationship at the narrowest pattern of time scale was identified in detail. **Figure S11-S12** shows the time series of daily RIR values at three sites in Zibo, where the temporal trend of RIR values was consistent with that at weekly scale (**Figure 4**). Additionally, the time series of daily RIR_{NOx}/RIR_{AVOC} (**Figure S13**) showed more irregular variations in temporal trends during the entire campaign, though such temporal trends were overall consistent with that of weekly scale in **Figure 4 g-i**. In summary, the time series of RIR values from the daily scale can provide more informative variations and characteristics of O_3-precursor relationship in temporal trends.

Table 2 summarizes the number of days and proportions that were classified into the three photochemical regimes across each site and each pattern of time scale. Near-consistent proportions of O_3 formation regimes (using RIR_{NOx}/RIR_{AVOC} as a metric) were shown among multiple patterns of time scale, whereas a variability of proportion occurred among the three sites. The proportions of photochemical regimes changed accordingly along with the time scale varied from wider to narrower pattern. Taking TZ as an example, 20% (monthly) and 26% (daily) of the time was considered as VOC-limited regime. The number of days and proportions for photochemical regimes summarized at four patterns of time scales can reveal a more plausible and comprehensive variation in ozone formation chemistry. Compared with patterns of monthly and weekly scales, the results derived at a daily scale can reveal the temporal variability of photochemical regimes more comprehensively. Note that the photochemical regime proportion obtained from the day-to-day scale has an advantage due to the large number of statistical samples.

3.6 Comparison among different patterns of time scale

This section gives a more comprehensive understanding of the campaign-averaging O_3-precursor relationship by comparing the similarities and differences of the results from various patterns of time scale. The overall O_3-precursor relationship for the entire campaign can be quantified by averaging the RIR values from the individual simulation runs depending on the chosen time scale (e.g., five simulation runs for monthly scale in this study). Therefore, four sets of logical and comparable results can be derived to represent the campaign-averaging O_3-precursor relationship, as four patterns of time scale (i.e., five-month, monthly, weekly, and daily) were treated in this study.

Figure 6 shows the averaged RIR values of the major precursor groups at different patterns of time scale. As the time scale changed from wider (i.e., five-month scale) to narrower (i.e., daily scale) pattern, all three sites showed increases in the means of RIR_{AVOC} and $RIR_{alkenes*}$ as well as decreases in averaged RIR_{NOx}, whereas the averaged RIR of other precursors (i.e., BVOC, CO, alkanes and aromatics) did not vary obviously (see **Table S6**). Comparing with the O_3-VOC-NO_x sensitivity at the daily scale, the results obtained at the five-month scale underestimated O_3-AVOC sensitivity (indicated by averaged RIR values) by 48% (TZ), 66% (BJ), and 49% (XD), and overestimated O_3-NO_x sensitivity by 37% (TZ), 142% (BJ), and 144% (XD). We performed comprehensive uncertainty analysis for model input and output results, which was assessed through statistical methods (see details in **Section 3.7**). We found that the model-derived RIR values may become more uncertain when the input dataset was averaged into a wider diurnal pattern (i.e., five-month scale), which may explain the discrepancy of RIR values between five-month scale and daily scale. We expect that

such discrepancies derived from different patterns of time scale could widely exist in many other world areas. Note that the mean RIR values were generally consistent among the four patterns of time scale within a reasonable range (within 25-75th quantile and standard deviation, see **Figure 6** and **Table S4**), suggesting that any selected pattern of time scale could reasonably derive the campaign-averaging O_3-precursor relationship.

Figure 7 further shows the variations in photochemical regimes (defined by RIR_{NOx}/RIR_{AVOC}; see **Text S2** and **Table S4** for details) for each pattern of time scale. Specifically, TZ was mainly considered as transitional regime for the entire campaign period, whereas its variations covered three photochemical regimes, which was consistent with the results from **Table S6**. BJ was generally identified as VOC-limited regime, whereas some days were also grouped into transitional regime. XD was considered as primarily between VOC-limited and transitional regime, and its variations also spanned three photochemical regimes. Compared with the five-month pattern, it was further found that the averaged RIR_{NOx}/RIR_{AVOC} from other time scale patterns (i.e., monthly, weekly, and daily) were higher (12% to 20% for TZ; 38% to 153% for XD) or lower (21% to 65% for BJ) than that from five-month scale. Note that the above discrepancies in photochemical regime derived from multiple patterns of time scale may influence the development of targeted O_3 control strategies. In summary, the photochemical regime derived by averaging RIR_{NOx}/RIR_{AVOC} from the daily scale (see **Table S6**) suggests that the three sites mainly followed the sequence of TZ (1.34 ± 1.39) > XD (0.67 ± 1.49) > BJ (0.16 ± 0.65).

In addition, the temporal variations of $TVOC/NO_x$ in different timescales were identified during the whole campaign, and good correlations between observed $TVOC/NO_x$ and model derived RIR_{NOx}/RIR_{AVOC} at four patterns of time scale were also found (see **Figure 5**). Such consistency suggests that both metrics can reasonably reflect the variation of photochemical regimes, which can also improve the reliability of our box model simulation.

The consistency and difference of model output (summarized in **Table S7**) are quantified by the statistical methods of Pearson's correlation coefficient (Hu et al., 2018) and paired-samples *t*-test analysis (Wang et al., 2016). In particular, we assess and compare the degree of significance of differences among multiple patterns of time scale by the *p* values (a statistical significance assuming at $p < 0.05$) through paired-samples *t*-test and Wilcoxon matched-paired signed-rank test (non-parametric statistics) (Chiclana et al., 2013). **Figure 8a** shows high Pearson's correlation coefficients (with values all above 0.85, $p < 0.01$) were found among four patterns of time scale, and the higher correlation coefficient was identified between the two closer patterns. **Figure 8b-c** shows that the differences among multiple patterns of time scale were non-significant using Paired-samples t-test analysis and Wilcoxon matched-pair signed-rank test respectively. Furthermore, their results indicate that more significant difference was

recognized between the two distant patterns (e.g., daily and five-month), which is consistent with the results of Pearson's correlation analysis. Noted that the discrepancy between the two distant patterns was not significant but non-negligible (e.g., $p = 0.092$ of Wilcoxon matched-paired signed-rank test between five-month and daily patterns).

The influence of different patterns of time scale on deriving RIR values from individual AVOC species was further investigated. Briefly, quantifying the relative contribution of individual AVOC on O_3 formation based on RIR calculation is beneficial to the development of cost-effective AVOC control strategies (Zhang et al., 2021). **Figure 9** shows the averaged RIR values of individual AVOC species (i.e., top 10) at different patterns of time scale (i.e., five-month, month-to-month, week-to-week) at three sites in Zibo. As shown in **Figure 9**, the 10 individual AVOC species at the three sites were selected according to the top 10 highest RIR from five-month pattern. All three sites showed that the RIR of individual AVOC species increased gradually as the time scale changed from the wider (i.e., five-month) to narrower (i.e., weekly) pattern, which was consistent with the earlier discussion (see **Figure 6** and **Table S6**) of O_3-AVOC sensitivity derived from four patterns of time scale. The results also indicate that the choice of time scale pattern has a limited effect on deriving high-ranking AVOC species (i.e., top 10) based on RIR calculations.

3.7 Uncertainty analysis

The uncertainty of model input was quantified in this section, which is embedded in pre-processed dataset with multiple patterns of time scale. As showed in **Figure 1**, the daily simulation used the individual daily pattern to constrain model, while the input dataset of averaged diurnal patterns (i.e., weekly, monthly, and five-month) is treated by averaging individual daily pattern into different timescales. This averaging approach will conceal the temporal variations of O_3 precursors and meteorological factors, particularly for a long-term observational campaign. **Figure S14** shows the distributions of the standard deviations for OH reactivity (k_{OH}) or concentration of O_3 precursor groups at three averaged patterns of time scale at the three sites. As the time scale changed from wider (i.e., five-month scale) to narrower (i.e., weekly scale) pattern, the uncertainty (indicated by the average, median and 25%-75% quantile) decreased accordingly. In addition, meteorological factors such as temperature and irradiation also play an important role on O_3 formation, especially these meteorological parameters can vary greatly over a long observational period (Boleti et al., 2020; Liu et al., 2019b; Weng et al., 2022). Therefore, the masked temporal variation of these meteorological factors behind the averaged input dataset would also result in model uncertainty.

Moreover, it has been widely recognized that the uncertainty for 0-D box model simulation mainly arises from the constraint of observation dataset and the configuration of model scheme. Note that constraints with more species from

measurements (or including as many species as possible) would lower its uncertainty from the chemical box model simulation (Wolfe et al., 2011, 2016). Nevertheless, due to the measurement limitation in our field campaign, we are unable to measure some important atmospheric species (i.e., HONO and oxygenated VOC (OVOC)), and these may arise uncertainty in box model simulation. For instance, Xue et al., (2021) performed a sensitivity test for HONO constraint in their box model simulation, and they showed that without HONO constraint would lead to O_3 photochemical production rate decreasing by 42%. More recently, Wang et al., (2022) obtained a comprehensive VOC dataset at Guangzhou, and their results showed that box model simulation without OVOCs constraints would underestimate the productions of ROx and O_3. Besides, both gaseous HNO_3 and organic nitrates can result in interferences on NO_x measurement by chemiluminescence technique, which may arise uncertainty in our box modelling (Ge et al., 2022; Uno et al., 2017; Xu et al., 2013). Since the accurate NO_x measurement is essential in determining the photochemical regime, more in-depth studies on NO_x measurement uncertainty in box model simulation are required in the future. In addition, the parameter configuration of model scheme is essential to derive a reliable and valid model output, such as dilution rate as an important model technical parameter. We performed a stepwise sensitivity test for this parameter to obtain an optimized dilution rate, and assigned it to all non-constraint species, which can reduce uncertainty in box model simulation (see details in **Text S1**). Also, the dry and/or wet deposition of pollutants is an important atmospheric physical process, which has been mostly parameterized in emission-based chemical transport modeling but very limited in box model, as most of the primarily emitted species are already constrained from measurements. Xue et al., (2014) considered O_3 deposition into box model simulation, and their result showed negligible contribution of O_3 deposition to total O_3 destruction rates. As for this work, we are unable to consider the deposition due to the difficulty in representing and parameterizing this term in the 0-D box model. Nevertheless, deposition of O_3 and other species may be one of the uncertainties during box model simulation, which is worth further study in the future.

4 Summary and implications

Our present results suggest that comprehensively understanding of multiple patterns of time scale is conductive to formulating a more accurate and robust O_3 control strategy. Specifically, as identified from the narrower patterns of time scale (i.e., weekly and daily), the site-to-site photochemical regime indicated by RIR_{NOx}/RIR_{AVOC} showed various magnitudes but a synchronous temporal trend. This indicates that the O_3 formation regime in a city area can be influenced by local and regional emissions jointly. The reason behind this phenomenon is not clear at present, and we believe that further investigation on the synergetic effect of local and regional emission reduction for O_3

control would help elucidating this observation. It was also found that the campaign-averaging photochemical regimes showed overall consistency but non-negligible variability among the four patterns of time scale, which was mainly due to the embedded uncertainty in model input dataset with averaged diurnal patterns. This implies that comparison among multiple patterns of time scale based on RIR analysis is useful to derive the O_3-precursor relationship more accurately and reliably.

Moreover, the high-ranking AVOC species (i.e., top 10) based on RIR calculations were overall consistent from the narrow to wide patterns of time scale. **Table S8** summarizes the total run number of box model for different patterns of time scale. It is known that large-scale computing capacity and computational efficiency were required in the narrower pattern of time scale (e.g., 2760 simulation runs in weekly scale in this study). Considering the difficulties of performing long-term and continuous online measurements in some environments, it is also advisable to identify the high-ranking VOC species from the campaign-averaging diurnal pattern in box model simulation.

In this study, we explored the non-linearity of O_3-precursor relationship in a way driven by the actual daily / weekly / monthly variability around the distribution. Our results highlight the importance to quantitatively test the impact of different timescales on photochemical regime determination, as there is uncertainty embedded in model input dataset when averaging individual daily pattern into different timescales. Such understanding would be complementary in developing more accurate O_3 pollution control strategy, particularly as the long-term O_3-precursor observations (e.g., from several months to years) are becoming more available than before in many places of China. In addition, site-to-site differences of model-derived photochemical regimes also underlines the importance of developing target O_3 control strategy for different areas in a city scale. Specifically, according to the averaged RIR_{NOx}/RIR_{AVOC} at daily pattern, the derived photochemical regime was transitional for TZ (suburban) and XD (suburban), while VOC-limited for BJ (urban). This implies that for mitigating ozone pollution in Zibo city, more endeavors should be devoted to the anthropogenic VOC reduction in urban areas, while strengthening the synergetic mitigation of VOC and NO_x emissions at the same time in other suburban areas. Although the above implications for O_3 control were derived from a case study in a major prefecture-level city (Zibo) of northern China, the developed approach by integrating multiple patterns of time scale in the present work can be used to other regions, particularly the on-going "One City One Policy" campaign (2021-2023) for O_3 control in many cities in China.

Acknowledgement

This work was supported by National Center for Air Pollution Prevention and Control (No. DQGG202119) and Ministry of Science and Technology PRC (No. G20200160001, No. G2021060002L). We also thank Prof. William Bloss for helpful comments.

Data and code availability

The code for the Master Chemical Mechanism (MCMv3.3.1) can be achieved from http://mcm.york.ac.uk/. The datasets generated during and/or analysed during the current study are available from the corresponding author on reasonable request.

Author contribution

KL conceived the study; ZZ performed the modeling; ZZ, KL, and ZB analyzed the data; BX, JD, LL, SL, CG, and WY conducted the field measurement; ZZ and KL wrote the paper with assistance of interpretation and revision from all authors. All authors contributed to the manuscript preparation and discussions.

Conflicts of interest

The authors declare that they have no conflicts of interest.

Supplement

The supplementary discussion of RIR calculation of different hypothetical changes, determining the photochemical regime, sensitivity test of different dilution rates, and detailed box modeling results are provided in **Text S1-S2**, **Table S1-S8** and **Figure S1-S18**.

References

Blanchard, C. L.: Ozone process insights from field experiments – Part III: extent of reaction and ozone formation, Atmos. Environ., 34(12), 2035–2043, doi:https://doi.org/10.1016/S1352-2310(99)00458-6, 2000.

Boleti, E., Hueglin, C., Grange, S. K., Prévôt, A. S. H. and Takahama, S.: Temporal and spatial analysis of ozone concentrations in Europe based on timescale decomposition and a multi-clustering approach, Atmos. Chem. Phys., 20(14), 9051–9066, doi:10.5194/acp-20-9051-2020, 2020.

Brunekreef, B. and Holgate, S. T.: Air pollution and health, Lancet, 360(9341), 1233–1242, doi:10.1016/S0140-6736(02)11274-8, 2002.

Cardelino, C. A. and Chameides, W. L.: An observation-based model for analyzing ozone precursor relationships in the urban atmosphere, J. Air Waste Manag. Assoc., 45(3), 161–180, doi:10.1080/10473289.1995.10467356, 1995.

Carter, W. P. L.: Development of the SAPRC-07 chemical mechanism, Atmos. Environ., 44(40), 5324–5335, doi:https://doi.org/10.1016/j.atmosenv.2010.01.026, 2010.

Cheng, H., Guo, H., Wang, X., Saunders, S. M., Lam, S. H. M., Jiang, F., Wang, T., Ding, A., Lee, S. and Ho, K. F.: On the relationship between ozone and its precursors in the Pearl River Delta: Application of an observation-based model (OBM), Environ. Sci. Pollut. Res., 17(3), 547–560, doi:10.1007/s11356-009-0247-9, 2010.

Chiclana, F., García, J. M. T., del Moral, M. J. and Herrera-Viedma, E.: A statistical comparative study of different similarity measures of consensus in group decision making, Inf. Sci. (Ny)., 221, 110–123, 2013.

Chien, Y.-C.: Variations in amounts and potential sources of volatile organic chemicals in new cars, Sci. Total Environ., 382(2), 228–239, doi:https://doi.org/10.1016/j.scitotenv.2007.04.022, 2007.

Council, N. R.: Rethinking the Ozone Problem in Urban and Regional Air Pollution, The National Academies Press, Washington, DC., 1991.

Fan, M. Y., Zhang, Y. L., Lin, Y. C., Li, L., Xie, F., Hu, J., Mozaffar, A. and Cao, F.: Source apportionments of atmospheric volatile organic compounds in Nanjing, China during high ozone pollution season, Chemosphere, 263, 128025, doi:10.1016/j.chemosphere.2020.128025, 2021.

Ge, D., Nie, W., Sun, P., Liu, Y., Wang, T., Wang, J., Wang, J., Wang, L., Zhu, C. and Wang, R.: Characterization of particulate organic nitrates in the Yangtze River Delta, East China, using the time-of-flight aerosol chemical speciation monitor, Atmos. Environ., 272, 118927, 2022.

Goliff, W. S., Stockwell, W. R. and Lawson, C. V: The regional atmospheric chemistry mechanism, version 2, Atmos. Environ., 68, 174–185, doi:https://doi.org/10.1016/j.atmosenv.2012.11.038, 2013.

He, Z., Wang, X., Ling, Z., Zhao, J., Guo, H., Shao, M. and Wang, Z.: Contributions of

different anthropogenic volatile organic compound sources to ozone formation at a receptor site in the Pearl River Delta region and its policy implications, Atmos. Chem. Phys., 19(13), 8801–8816, doi:10.5194/acp-19-8801-2019, 2019a.
He, Z., Wang, X., Ling, Z., Zhao, J., Guo, H., Shao, M. and Wang, Z.: Contributions of different anthropogenic volatile organic compound sources to ozone formation at a receptor site in the Pearl River Delta region and its policy implications, Atmos. Chem. Phys., 19(13), 8801–8816, doi:10.5194/acp-19-8801-2019, 2019b.
Hidy, G. M.: Ozone process insights from field experiments - part I: Overview, Atmos. Environ., 34(12–14), 2001–2022, doi:10.1016/S1352-2310(99)00456-2, 2000.
Hu, H., Landgraf, J., Detmers, R., Borsdorff, T., Aan de Brugh, J., Aben, I., Butz, A. and Hasekamp, O.: Toward global mapping of methane with TROPOMI: First results and intersatellite comparison to GOSAT, Geophys. Res. Lett., 45(8), 3682–3689, 2018.
Jenkin, M. E., Young, J. C. and Rickard, A. R.: The MCM v3.3.1 degradation scheme for isoprene, Atmos. Chem. Phys., 15(20), 11433–11459, doi:10.5194/acp-15-11433-2015, 2015.
Jiang, M., Lu, K., Su, R., Tan, Z., Wang, H., Li, L., Fu, Q., Zhai, C., Tan, Q. and Yue, D.: Ozone formation and key VOCs in typical Chinese city clusters, Chinese Sci. Bull., 63(12), 1130–1141, 2018.
Kleinman, L. I.: Ozone process insights from field experiments – part II: Observation-based analysis for ozone production, Atmos. Environ., 34(12), 2023–2033, doi:https://doi.org/10.1016/S1352-2310(99)00457-4, 2000.
Li, J., Zhai, C., Yu, J., Liu, R., Li, Y., Zeng, L. and Xie, S.: Spatiotemporal variations of ambient volatile organic compounds and their sources in Chongqing, a mountainous megacity in China, Sci. Total Environ., 627, 1442–1452, 2018.
Li, K., Jacob, D. J., Liao, H., Shen, L., Zhang, Q. and Bates, K. H.: Anthropogenic drivers of 2013–2017 trends in summer surface ozone in China, Proc. Natl. Acad. Sci., 116(2), 422 LP – 427, doi:10.1073/pnas.1812168116, 2019.
Li, K., Wang, X., Li, L., Wang, J., Liu, Y., Cheng, X., Xu, B., Wang, X., Yan, P., Li, S., Geng, C., Yang, W., Azzi, M. and Bai, Z.: Large variability of O3-precursor relationship during severe ozone polluted period in an industry-driven cluster city (Zibo) of North China Plain, J. Clean. Prod., 316, 128252, doi:https://doi.org/10.1016/j.jclepro.2021.128252, 2021.
Lin, H., Wang, M., Duan, Y., Fu, Q., Ji, W., Cui, H., Jin, D., Lin, Y. and Hu, K.: O3 sensitivity and contributions of different nmhc sources in O3 formation at urban and suburban sites in Shanghai, Atmosphere (Basel)., 11(3), 295, 2020.
Ling, Z. H., Guo, H., Cheng, H. R. and Yu, Y. F.: Sources of ambient volatile organic compounds and their contributions to photochemical ozone formation at a site in the Pearl River Delta, southern China, Environ. Pollut., 159(10), 2310–2319, doi:10.1016/j.envpol.2011.05.001, 2011.
Liu, X., Lyu, X., Wang, Y., Jiang, F. and Guo, H.: Intercomparison of O3 formation and radical chemistry in the past decade at a suburban site in Hong Kong, Atmos.

669 Chem. Phys., 19(7), 5127–5145, doi:10.5194/acp-19-5127-2019, 2019a.
670 Liu, X., Lyu, X., Wang, Y., Jiang, F. and Guo, H.: Intercomparison of O3 formation
671 and radical chemistry in the past decade at a suburban site in Hong Kong, Atmos.
672 Chem. Phys., 19(7), 5127–5145, doi:10.5194/acp-19-5127-2019, 2019b.
673 Liu, X., Wang, N., Lyu, X., Zeren, Y., Jiang, F., Wang, X., Zou, S., Ling, Z. and Guo,
674 H.: Photochemistry of ozone pollution in autumn in Pearl River Estuary, South
675 China, Sci. Total Environ., 754, 141812,
676 doi:https://doi.org/10.1016/j.scitotenv.2020.141812, 2021a.
677 Liu, X., Wang, N., Lyu, X., Zeren, Y., Jiang, F., Wang, X., Zou, S., Ling, Z. and Guo,
678 H.: Photochemistry of ozone pollution in autumn in Pearl River Estuary, South
679 China, Sci. Total Environ., 754, doi:10.1016/j.scitotenv.2020.141812, 2021b.
680 Lu, H., Lyu, X., Cheng, H., Ling, Z., Guo, H. and Lu, H.: Overview on the spatial–
681 temporal characteristics of the ozone formation regime in China, Environ. Sci., v.
682 21(6), 916-929–2019 v.21 no.6, doi:10.1039/c9em00098d, 2019.
683 Lu, K., Zhang, Y., Su, H., Brauers, T., Chou, C. C., Hofzumahaus, A., Liu, S. C., Kita,
684 K., Kondo, Y., Shao, M., Wahner, A., Wang, J., Wang, X. and Zhu, T.: Oxidant
685 (O3 + NO2) production processes and formation regimes in Beijing, J. Geophys.
686 Res. Atmos., 115(7), 1–18, doi:10.1029/2009JD012714, 2010a.
687 Lu, K., Zhang, Y., Su, H., Shao, M., Zeng, L., Zhong, L., Xiang, Y., Chang, C., Chou,
688 C. K. C. and Wahner, A.: Regional ozone pollution and key controlling factors of
689 photochemical ozone production in Pearl River Delta during summer time, Sci.
690 China Chem., 53(3), 651–663, doi:10.1007/s11426-010-0055-6, 2010b.
691 Lu, X., Hong, J., Zhang, L., Cooper, O. R., Schultz, M. G., Xu, X., Wang, T., Gao, M.,
692 Zhao, Y. and Zhang, Y.: Severe Surface Ozone Pollution in China: A Global
693 Perspective, Environ. Sci. Technol. Lett., 5(8), 487–494,
694 doi:10.1021/acs.estlett.8b00366, 2018.
695 Lyu, X., Wang, N., Guo, H., Xue, L., Jiang, F., Zeren, Y., Cheng, H., Cai, Z., Han, L.
696 and Zhou, Y.: Causes of a continuous summertime O3 pollution event in Jinan, a
697 central city in the North China Plain, Atmos. Chem. Phys., 19(5), 3025–3042,
698 doi:10.5194/acp-19-3025-2019, 2019a.
699 Lyu, X., Wang, N., Guo, H., Xue, L., Jiang, F., Zeren, Y., Cheng, H., Cai, Z., Han, L.
700 and Zhou, Y.: Causes of a continuous summertime O3 pollution event in Jinan, a
701 central city in the North China Plain, Atmos. Chem. Phys., 19(5), 3025–3042,
702 doi:10.5194/acp-19-3025-2019, 2019b.
703 Lyu, X. P., Chen, N., Guo, H., Zhang, W. H., Wang, N., Wang, Y. and Liu, M.: Ambient
704 volatile organic compounds and their effect on ozone production in Wuhan, central
705 China, Sci. Total Environ., 541, 200–209,
706 doi:https://doi.org/10.1016/j.scitotenv.2015.09.093, 2016a.
707 Lyu, X. P., Chen, N., Guo, H., Zhang, W. H., Wang, N., Wang, Y. and Liu, M.: Ambient
708 volatile organic compounds and their effect on ozone production in Wuhan, central
709 China, Sci. Total Environ., 541, 200–209, doi:10.1016/j.scitotenv.2015.09.093,
710 2016b.

Qin, M., Chen, Z., Shen, H., Li, H., Wu, H. and Wang, Y.: Impacts of heterogeneous reactions to atmospheric peroxides: Observations and budget analysis study, Atmos. Environ., 183(April), 144–153, doi:10.1016/j.atmosenv.2018.04.005, 2018.

Saunders, S. M., Jenkin, M. E., Derwent, R. G. and Pilling, M. J.: Protocol for the development of the Master Chemical Mechanism, MCM v3 (Part A): Tropospheric degradation of non-aromatic volatile organic compounds, Atmos. Chem. Phys., 3(1), 161–180, doi:10.5194/acp-3-161-2003, 2003.

Sicard, P., De Marco, A., Agathokleous, E., Feng, Z., Xu, X., Paoletti, E., Rodriguez, J. J. D. and Calatayud, V.: Amplified ozone pollution in cities during the COVID-19 lockdown, Sci. Total Environ., 735, doi:10.1016/j.scitotenv.2020.139542, 2020.

Sillman, S.: Observation-Based Methods (OBMS) For Analyzing Urban/Regional Ozone Production And Ozone-NO_x-VOC Sensitivity, , (x), 1–44 [online] Available from: http://www-personal.engin.umich.edu/~sillman, 2010.

Stockwell, W. R., Kirchner, F., Kuhn, M. and Seefeld, S.: A new mechanism for regional atmospheric chemistry modeling, J. Geophys. Res. Atmos., 102(22), doi:10.1029/97jd00849, 1997.

Stockwell, W. R., Saunders, E., Goliff, W. S. and Fitzgerald, R. M.: A perspective on the development of gas-phase chemical mechanisms for Eulerian air quality models, J. Air Waste Manage. Assoc., 70(1), 44–70, 2020.

Su, R., Lu, K., Yu, J., Tan, Z., Jiang, M., Li, J., Xie, S., Wu, Y., Zeng, L. and Zhai, C.: Exploration of the formation mechanism and source attribution of ambient ozone in Chongqing with an observation-based model, Sci. China Earth Sci., 61(1), 23–32, 2018a.

Su, R., Lu, K. D., Yu, J. Y., Tan, Z. F., Jiang, M. Q., Li, J., Xie, S. D., Wu, Y. S., Zeng, L. M., Zhai, C. Z. and Zhang, Y. H.: Exploration of the formation mechanism and source attribution of ambient ozone in Chongqing with an observation-based model, Sci. China Earth Sci., 61(1), 23–32, doi:10.1007/s11430-017-9104-9, 2018b.

Sun, L., Xue, L., Wang, T., Gao, J., Ding, A., Cooper, O. R., Lin, M., Xu, P., Wang, Z., Wang, X., Wen, L., Zhu, Y., Chen, T., Yang, L., Wang, Y., Chen, J. and Wang, W.: Significant increase of summertime ozone at Mount Tai in Central Eastern China, Atmos. Chem. Phys., 16(16), 10637–10650, doi:10.5194/acp-16-10637-2016, 2016.

Tan, Z., Lu, K., Dong, H., Hu, M., Li, X., Liu, Y., Lu, S., Shao, M., Su, R. and Wang, H.: Explicit diagnosis of the local ozone production rate and the ozone-NO_x-VOC sensitivities, Sci. Bull., 63(16), 1067–1076, 2018a.

Tan, Z., Lu, K., Jiang, M., Su, R., Dong, H., Zeng, L., Xie, S., Tan, Q. and Zhang, Y.: Exploring ozone pollution in Chengdu, southwestern China: A case study from radical chemistry to O3-VOC-NO_x sensitivity, Sci. Total Environ., 636, 775–786, 2018b.

Tan, Z., Lu, K., Jiang, M., Su, R., Wang, H., Lou, S., Fu, Q., Zhai, C., Tan, Q. and Yue, D.: Daytime atmospheric oxidation capacity in four Chinese megacities during the photochemically polluted season: a case study based on box model simulation, Atmos. Chem. Phys., 19(6), 3493–3513, 2019a.

753 Tan, Z., Lu, K., Jiang, M., Su, R., Wang, H., Lou, S., Fu, Q., Zhai, C., Tan, Q., Yue, D.,
754 Chen, D., Wang, Z., Xie, S., Zeng, L. and Zhang, Y.: Daytime atmospheric
755 oxidation capacity in four Chinese megacities during the photochemically polluted
756 season: A case study based on box model simulation, Atmos. Chem. Phys., 19(6),
757 3493–3513, doi:10.5194/acp-19-3493-2019, 2019b.
758 Uno, I., Osada, K., Yumimoto, K., Wang, Z., Itahashi, S., Pan, X., Hara, Y., Kanaya,
759 Y., Yamamoto, S. and Fairlie, T. D.: Seasonal variation of fine-and coarse-mode
760 nitrates and related aerosols over East Asia: synergetic observations and chemical
761 transport model analysis, Atmos. Chem. Phys., 17(23), 14181–14197, 2017.
762 Vingarzan, R.: A review of surface ozone background levels and trends, Atmos.
763 Environ., 38(21), 3431–3442, 2004.
764 Wang, H., Hu, X. and Sterba-Boatwright, B.: A new statistical approach for interpreting
765 oceanic fCO2 data, Mar. Chem., 183, 41–49, 2016.
766 Wang, M., Hu, K., Chen, W., Shen, X., Li, W. and Lu, X.: Ambient Non-Methane
767 Hydrocarbons (NMHCs) Measurements in Baoding, China: Sources and Roles in
768 Ozone Formation, Atmosphere (Basel)., 11(11), 1205, 2020a.
769 Wang, P., Chen, Y., Hu, J., Zhang, H. and Ying, Q.: Attribution of Tropospheric Ozone
770 to NO x and VOC Emissions: Considering Ozone Formation in the Transition
771 Regime, Environ. Sci. Technol., 53(3), 1404–1412, doi:10.1021/acs.est.8b05981,
772 2019.
773 Wang, T., Xue, L., Brimblecombe, P., Lam, Y. F., Li, L. and Zhang, L.: Ozone pollution
774 in China: A review of concentrations, meteorological influences, chemical
775 precursors, and effects, Sci. Total Environ., 575, 1582–1596,
776 doi:10.1016/j.scitotenv.2016.10.081, 2017a.
777 Wang, T., Xue, L., Brimblecombe, P., Lam, Y. F., Li, L. and Zhang, L.: Ozone pollution
778 in China: A review of concentrations, meteorological influences, chemical
779 precursors, and effects, Sci. Total Environ., 575, 1582–1596, 2017b.
780 Wang, W., Yuan, B., Peng, Y., Su, H., Cheng, Y., Yang, S., Wu, C., Qi, J., Bao, F. and
781 Huangfu, Y.: Direct observations indicate photodegradable oxygenated volatile
782 organic compounds (OVOCs) as larger contributors to radicals and ozone
783 production in the atmosphere, Atmos. Chem. Phys., 22(6), 4117–4128, 2022.
784 Wang, Y., Wang, H., Guo, H., Lyu, X., Cheng, H., Ling, Z., Louie, P. K. K., Simpson,
785 I. J., Meinardi, S. and Blake, D. R.: Long-term O 3–precursor relationships in Hong
786 Kong: field observation and model simulation, Atmos. Chem. Phys., 17(18),
787 10919–10935, 2017c.
788 Wang, Y., Wang, H., Guo, H., Lyu, X., Cheng, H., Ling, Z., Louie, P. K. K., Simpson,
789 I. J., Meinardi, S. and Blake, D. R.: Long-term O3-precursor relationships in Hong
790 Kong: Field observation and model simulation, Atmos. Chem. Phys., 17(18),
791 10919–10935, doi:10.5194/acp-17-10919-2017, 2017d.
792 Wang, Y., Guo, H., Zou, S., Lyu, X., Ling, Z., Cheng, H. and Zeren, Y.: Surface O3
793 photochemistry over the South China Sea: Application of a near-explicit chemical
794 mechanism box model, Environ. Pollut., 234, 155–166,

795 doi:10.1016/j.envpol.2017.11.001, 2018.
796 Wang, Y., Gao, W., Wang, S., Song, T., Gong, Z., Ji, D., Wang, L., Liu, Z., Tang, G.,
797 Huo, Y., Tian, S., Li, J., Li, M., Yang, Y., Chu, B., Petäjä, T., Kerminen, V. M., He,
798 H., Hao, J., Kulmala, M., Wang, Y. and Zhang, Y.: Contrasting trends of PM2.5and
799 surface-ozone concentrations in China from 2013 to 2017, Natl. Sci. Rev., 7(8),
800 1331–1339, doi:10.1093/nsr/nwaa032, 2020b.
801 Weng, X., Forster, G. L. and Nowack, P.: A machine learning approach to quantify
802 meteorological drivers of ozone pollution in China from 2015 to 2019, Atmos.
803 Chem. Phys., 22(12), 8385–8402, doi:10.5194/acp-22-8385-2022, 2022.
804 Whalley, L. K., Slater, E. J., Woodward-Massey, R., Ye, C., Lee, J. D., Squires, F.,
805 Hopkins, J. R., Dunmore, R. E., Shaw, M. and Hamilton, J. F.: Evaluating the
806 sensitivity of radical chemistry and ozone formation to ambient VOCs and NO x in
807 Beijing, Atmos. Chem. Phys., 21(3), 2125–2147, 2021a.
808 Whalley, L. K., Slater, E. J., Woodward-Massey, R., Ye, C., Lee, J. D., Squires, F.,
809 Hopkins, J. R., Dunmore, R. E., Shaw, M., Hamilton, J. F., Lewis, A. C., Mehra,
810 A., Worrall, S. D., Bacak, A., Bannan, T. J., Coe, H., Percival, C. J., Ouyang, B.,
811 Jones, R. L., Crilley, L. R., Kramer, L. J., Bloss, W. J., Vu, T., Kotthaus, S.,
812 Grimmond, S., Sun, Y., Xu, W., Yue, S., Ren, L., Joe, W., Nicholas Hewitt, C.,
813 Wang, X., Fu, P. and Heard, D. E.: Evaluating the sensitivity of radical chemistry
814 and ozone formation to ambient VOCs and NO_x in Beijing, Atmos. Chem. Phys.,
815 21(3), 2125–2147, doi:10.5194/acp-21-2125-2021, 2021b.
816 Willmott, C. J.: Some comments on the evaluation of model performance., Bull. - Am.
817 Meteorol. Soc., 63(11), 1309–1313, doi:10.1175/1520-
818 0477(1982)063<1309:SCOTEO>2.0.CO;2, 1982.
819 Wolfe, G. M., Thornton, J. A., Bouvier-Brown, N. C., Goldstein, A. H., Park, J.-H.,
820 McKay, M., Matross, D. M., Mao, J., Brune, W. H. and LaFranchi, B. W.: The
821 Chemistry of Atmosphere-Forest Exchange (CAFE) model–part 2: application to
822 BEARPEX-2007 observations, Atmos. Chem. Phys., 11(3), 1269–1294, 2011.
823 Wolfe, G. M., Marvin, M. R., Roberts, S. J., Travis, K. R. and Liao, J.: The framework
824 for 0-D atmospheric modeling (F0AM) v3. 1, Geosci. Model Dev., 9(9), 3309–3319,
825 2016.
826 Xie, X., Shao, M., Liu, Y., Lu, S., Chang, C.-C. and Chen, Z.-M.: Estimate of initial
827 isoprene contribution to ozone formation potential in Beijing, China, Atmos.
828 Environ., 42(24), 6000–6010, 2008.
829 Xu, Z., Wang, T., Xue, L. K., Louie, P. K. K., Luk, C. W. Y., Gao, J., Wang, S. L.,
830 Chai, F. H. and Wang, W. X.: Evaluating the uncertainties of thermal catalytic
831 conversion in measuring atmospheric nitrogen dioxide at four differently polluted
832 sites in China, Atmos. Environ., 76, 221–226, 2013.
833 Xu, Z., Huang, X., Nie, W., Chi, X., Xu, Z., Zheng, L., Sun, P. and Ding, A.: Influence
834 of synoptic condition and holiday effects on VOCs and ozone production in the
835 Yangtze River Delta region, China, Atmos. Environ., 168, 112–124, 2017.
836 Xue, L., Wang, T., Louie, P. K. K., Luk, C. W. Y., Blake, D. R. and Xu, Z.: Increasing

external effects negate local efforts to control ozone air pollution: a case study of Hong Kong and implications for other Chinese cities, Environ. Sci. Technol., 48(18), 10769–10775, 2014a.

Xue, L., Wang, T., Louie, P. K. K., Luk, C. W. Y., Blake, D. R. and Xu, Z.: Increasing external effects negate local efforts to control ozone air pollution: A case study of Hong Kong and implications for other chinese cities, Environ. Sci. Technol., 48(18), 10769–10775, doi:10.1021/es503278g, 2014b.

Xue, L. K., Wang, T., Gao, J., Ding, A. J., Zhou, X. H., Blake, D. R., Wang, X. F., Saunders, S. M., Fan, S. J., Zuo, H. C., Zhang, Q. Z. and Wang, W. X.: Ground-level ozone in four Chinese cities: Precursors, regional transport and heterogeneous processes, Atmos. Chem. Phys., 14(23), 13175–13188, doi:10.5194/acp-14-13175-2014, 2014c.

Xue, M., Ma, J., Tang, G., Tong, S., Hu, B., Zhang, X., Li, X. and Wang, Y.: ROx Budgets and O3 Formation during Summertime at Xianghe Suburban Site in the North China Plain, Adv. Atmos. Sci., 38(7), 1209–1222, 2021.

Xue, T., Zheng, Y., Geng, G., Xiao, Q., Meng, X., Wang, M., Li, X., Wu, N., Zhang, Q. and Zhu, T.: Estimating Spatiotemporal Variation in Ambient Ozone Exposure during 2013–2017 Using a Data-Fusion Model, Environ. Sci. Technol., 54(23), 14877–14888, 2020.

Yarwood, G., Rao, S., Yocke, M. and Whitten, G. Z.: Updates to the carbon bond chemical mechanism: CB05, Final Rep. to US EPA, RT-0400675, 8, 13, 2005.

Yarwood, G., Jung, J., Whitten, G. Z., Heo, G., Mellberg, J. and Estes, M.: Updates to the Carbon Bond mechanism for version 6 (CB6), in 9th Annual CMAS Conference, Chapel Hill, NC, pp. 11–13., 2010.

Yin, M., Zhang, X., Li, Y., Fan, K., Li, H., Gao, R. and Li, J.: Ambient ozone pollution at a coal chemical industry city in the border of Loess Plateau and Mu Us Desert: characteristics, sensitivity analysis and control strategies, PeerJ, 9, e11322, 2021.

Yu, D., Tan, Z., Lu, K., Ma, X., Li, X., Chen, S., Zhu, B., Lin, L., Li, Y., Qiu, P., Yang, X., Liu, Y., Wang, H., He, L., Huang, X. and Zhang, Y.: An explicit study of local ozone budget and NO_x-VOCs sensitivity in Shenzhen China, Atmos. Environ., 224, 117304, doi:https://doi.org/10.1016/j.atmosenv.2020.117304, 2020a.

Yu, D., Tan, Z., Lu, K., Ma, X., Li, X., Chen, S., Zhu, B., Lin, L., Li, Y., Qiu, P., Yang, X., Liu, Y., Wang, H., He, L., Huang, X. and Zhang, Y.: An explicit study of local ozone budget and NO_x-VOCs sensitivity in Shenzhen China, Atmos. Environ., 224(November 2019), 117304, doi:10.1016/j.atmosenv.2020.117304, 2020b.

Zeng, L., Lyu, X., Guo, H., Zou, S. and Ling, Z.: Photochemical Formation of C1-C5 Alkyl Nitrates in Suburban Hong Kong and over the South China Sea, Environ. Sci. Technol., 52(10), 5581–5589, doi:10.1021/acs.est.8b00256, 2018.

Zhang, Q., Zheng, Y., Tong, D., Shao, M., Wang, S., Zhang, Y., Xu, X., Wang, J., He, H., Liu, W., Ding, Y., Lei, Y., Li, J., Wang, Z., Zhang, X., Wang, Y., Cheng, J., Liu, Y., Shi, Q., Yan, L., Geng, G., Hong, C., Li, M., Liu, F., Zheng, B., Cao, J., Ding, A., Gao, J., Fu, Q., Huo, J., Liu, B., Liu, Z., Yang, F., He, K. and Hao, J.:

879 Drivers of improved PM2.5 air quality in China from 2013 to 2017, Proc. Natl.
880 Acad. Sci., 116(49), 24463 LP – 24469, doi:10.1073/pnas.1907956116, 2019.
881 Zhang, Y., Xue, L., Carter, W. P. L., Pei, C., Chen, T., Mu, J., Wang, Y., Zhang, Q. and
882 Wang, W.: Development of ozone reactivity scales for volatile organic compounds
883 in a Chinese megacity, Atmos. Chem. Phys., 21(14), 11053–11068,
884 doi:10.5194/acp-21-11053-2021, 2021.
885 Zhang, Y. H., Hu, M., Zhong, L. J., Wiedensohler, A., Liu, S. C., Andreae, M. O., Wang,
886 W. and Fan, S. J.: Regional Integrated Experiments on Air Quality over Pearl River
887 Delta 2004 (PRIDE-PRD2004): Overview, Atmos. Environ., 42(25), 6157–6173,
888 doi:10.1016/j.atmosenv.2008.03.025, 2008a.
889 Zhang, Y. H., Su, H., Zhong, L. J., Cheng, Y. F., Zeng, L. M., Wang, X. S., Xiang, Y.
890 R., Wang, J. L., Gao, D. F., Shao, M., Fan, S. J. and Liu, S. C.: Regional ozone
891 pollution and observation-based approach for analyzing ozone–precursor
892 relationship during the PRIDE-PRD2004 campaign, Atmos. Environ., 42(25),
893 6203–6218, doi:https://doi.org/10.1016/j.atmosenv.2008.05.002, 2008b.
894 Zhao, Y., Chen, L., Li, K., Han, L., Zhang, X., Wu, X., Gao, X., Azzi, M. and Cen, K.:
895 Atmospheric ozone chemistry and control strategies in Hangzhou, China:
896 Application of a 0-D box model, Atmos. Res., 246, 105109, 2020.
897 Zong, R., Yang, X., Wen, L., Xu, C., Zhu, Y., Chen, T., Yao, L., Wang, L., Zhang, J.,
898 Yang, L., Wang, X., Shao, M., Zhu, T., Xue, L. and Wang, W.: Strong ozone
899 production at a rural site in theNorth China Plain: Mixed effects of urban plumesand
900 biogenic emissions, J. Environ. Sci. (China), 71, 261–270,
901 doi:10.1016/j.jes.2018.05.003, 2018.
902

903 **Table 1.** Summary of relevant published 0-D box model studies in China.

City	Site/Type		Period	Patterns of Time scale[a]	Mechanism	Reference
Beijing	PKU[b]	Urban	10 Aug–10 Sep 2006	Day-to-day (25 d)	CB-IV	(Lu et al., 2010)
	YUFA	Suburban				
	PKU	Urban	13–29 Apr 2015, 11–29 Aug 2015, 22 Feb–12 Mar 2016	Entire period	RACM2	(Qin et al., 2018)
	Beijing	Urban	2–19 Jul 2014	Entire period	RACM2	(Tan et al., 2019b)
Dezhou	Yucheng	Rural	1 Jun–6 Jul 2013	Day-to-day (2 d)	MCMv3.3.1	(Zong et al., 2018)
Shenzhen	SYY[c]	Urban	28 Sep–31 Oct 2018	Entire period	RACM2	(Yu et al., 2020b)
	Fucheng	Urban				
Hong Kong	TC	Suburban	10 Aug–21 Oct 2013	Entire period	MCMv3.2	(Zeng et al., 2018)
	Wan Shan	Island				
	Tung Chung	Urban	Sep-Nov 2002, 2007, 2012	Year-to-year (3 yrs)	MCMv3.2	(Xue et al., 2014b)
	Qing Sha	Urban	23 Oct–1 Nov 2007	Day-to-day (10 d)	CB-IV	(Cheng et al., 2010)
	Tai O					
	Tung Chung	Urban	Jan 2005-Dec 2014	Month-to-month (5 months)	CB05	(Whalley et al., 2021b)
Chengdu	Pengzhou	Suburban	3 Sep–2 Oct 2016	Entire period	RACM2	(Tan et al., 2018b)
	Pixian	Suburban				
	Shuangliu	Suburban				
	Chengzhong	Urban				
Zhuhai	Qi'ao	Mountain	25 Sep–28 Oct 2016	Entire period	MCMv3.2	(Liu et al., 2021b)
Wuhan	HPEMC[d]	Urban	Feb 2013-Oct 2014	Month-to-month (21 months)	MCMv3.2	(Lyu et al., 2016)
Guangzhou	GZ	Urban	5–17 Jul 2006	Day-to-day (16 d)	CB-IV	(Lu et al., 2010)
	BZ	Suburban				
	Guangzhou	Urban	4 Oct–5 Nov 2004	Entire period	SAPRC	(Zhang et al., 2008b)
	Xinken	Nonurban				
Hangzhou	Zhaohui	Urban	17 May, 26 Jun 20, Jul 24, Aug and 26 Sep	Entire period (5 d)	MCMv3.3.1	(Zhao et al., 2020)
	Xiasha	Suburban				

	Huapu	Urban				
Nanjing	NUIST[e]	Suburban	3 Jul–1 Aug 2018	Entire period	CB-IV	(Fan et al., 2021)
	SORPES	Suburban	22 Sep–7 Oct 2014	Day-to-day (8 d)	MCMv3.3.1	(Xu et al., 2017)
Yulin	EMB[f]	Urban	7 Jul–10 Aug 2019	Day-to-day (13 d)	MCMv3.3.1	(Yin et al., 2021)
Lanzhou	Renshoushan Park	Urban	19 Jun–16 Jul 2006	Day-to-day (3 d)	MCMv3.2	(Xue et al., 2014)
Baoding	EPB[g]	Urban	10–30 Sep 2015	Day-to-day (5 d)	MCMv3.3.1	(Wang et al., 2020a)
Chongqing	Nan Quan	Suburban	24 Aug–22 Sep 2015	Day-to-day (7 d)	MCMv3.2	(Li et al., 2018)
	Chao Zhan	Urban				
	Jin Yun Shan	Urban				
Shanghai	Pudong	Urban	1–31 Jul 2017	Day-to-day (16 d)	CB-IV	(Lin et al., 2020)
	Dianshanhu	Suburban				
South China Sea	Wanshan	Island	11 Sep–21 Nov 2013	Entire period	MCMv3.2	(Wang et al., 2018)

[a]Number of days for modeling the patterns of time scale denotes that which was simulated by the box model.
[b]Peking University
[c]Shenzhen Yanjiusheng Yuan
[d]Hubei Provincial Environmental Monitoring Center
[e]Nanjing University of Information Science & Technology
[f]Environmental Monitoring Building
[g]Environmental Protection Bureau

904

905 **Table 2.** Summary of the number of days (for model calculation) and proportions that
906 were classified into the three photochemical regimes across each site and multiple
907 patterns of time scale.

Patterns of Time scale	Site	Photochemical regime: RIR_{NOx}/RIR_{AVOC}					
		NO_x-limited: >2		Transition: 0.5~2		VOC-limited: <0.5	
		No. of days	Proportion	No. of days	Proportion	No. of days	Proportion
Month-to-month	TZ	2	40%	2	40%	1	20%
	BJ	0	0%	3	60%	2	40%
	XD	0	0%	2	40%	3	60%
Week-to-week	TZ	7	33%	8	38%	6	29%
	BJ	0	0%	10	50%	10	50%
	XD	3	16%	6	32%	10	53%
Day-to-day	TZ	29	29%	45	45%	26	26%
	BJ	0	0%	21	26%	60	74%
	XD	20	18%	23	20%	71	62%

908

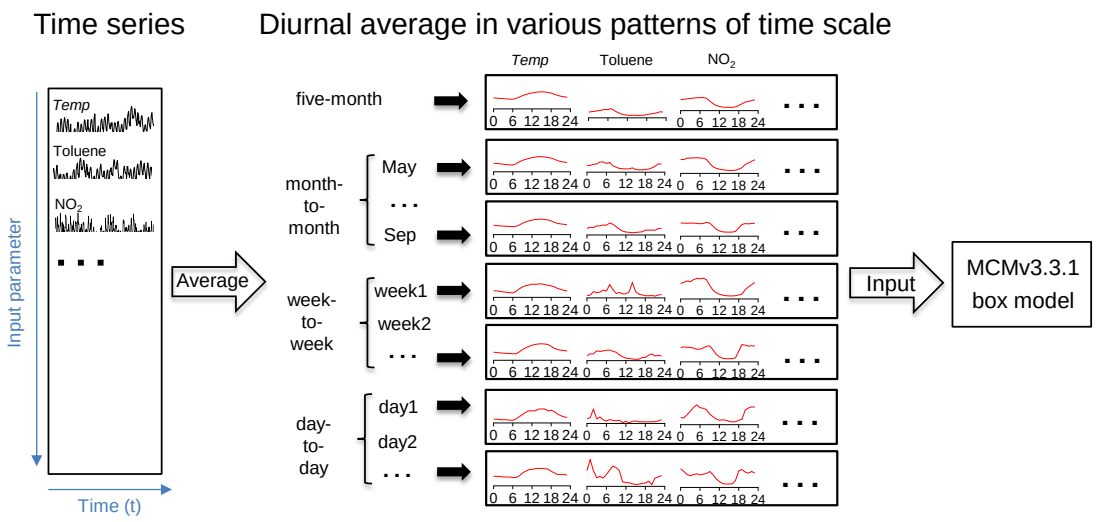

Figure 1. Schematic diagram of the dataset treatment to derive four patterns of time scale for 0-D box model input. Note that the four patterns (i.e., five-month, monthly, weekly, and daily) were the diurnal average of the initial dataset. This diagram takes one site and several input measurements (temperature, toluene, and NO_2) as examples.

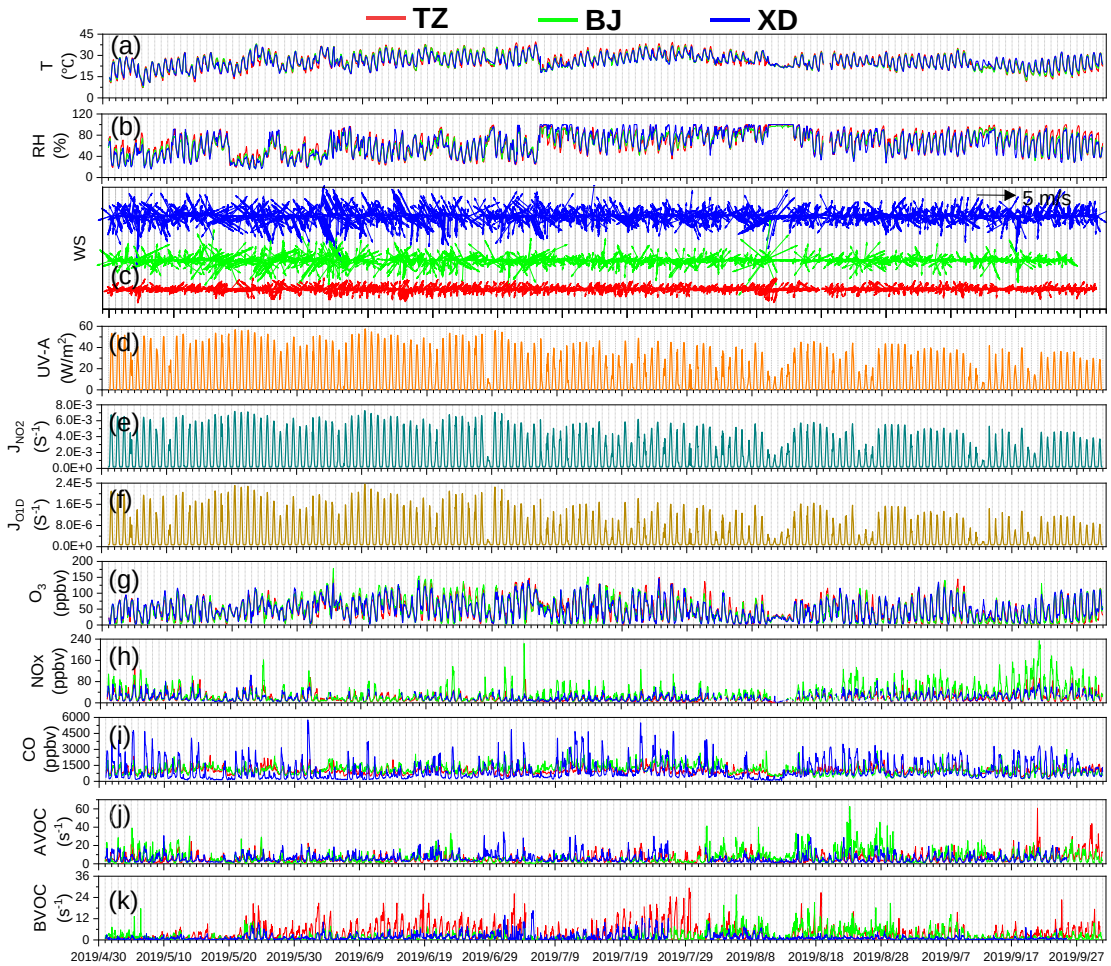

Figure 2. Time series of meteorological parameters, O_3 and its precursors (i.e., CO, NO_x, VOCs) throughout the whole campaign at the three sites in Zibo.

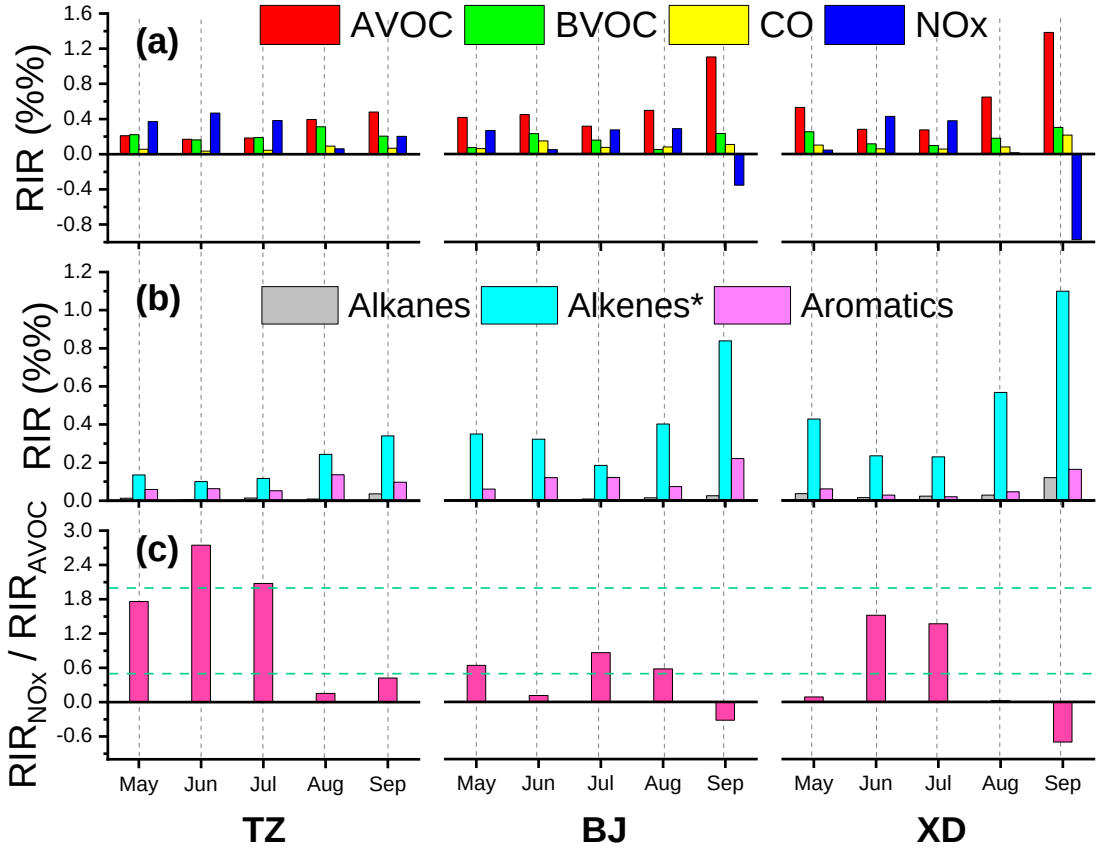

Figure 3. Time series of month-to-month RIR values of major precursor groups and RIR_{NOx}/RIR_{AVOC} at three sites (TZ, BJ and XD) in Zibo. The green dash line indicates to RIR_{NOx}/RIR_{AVOC} = 0.5 and 2.

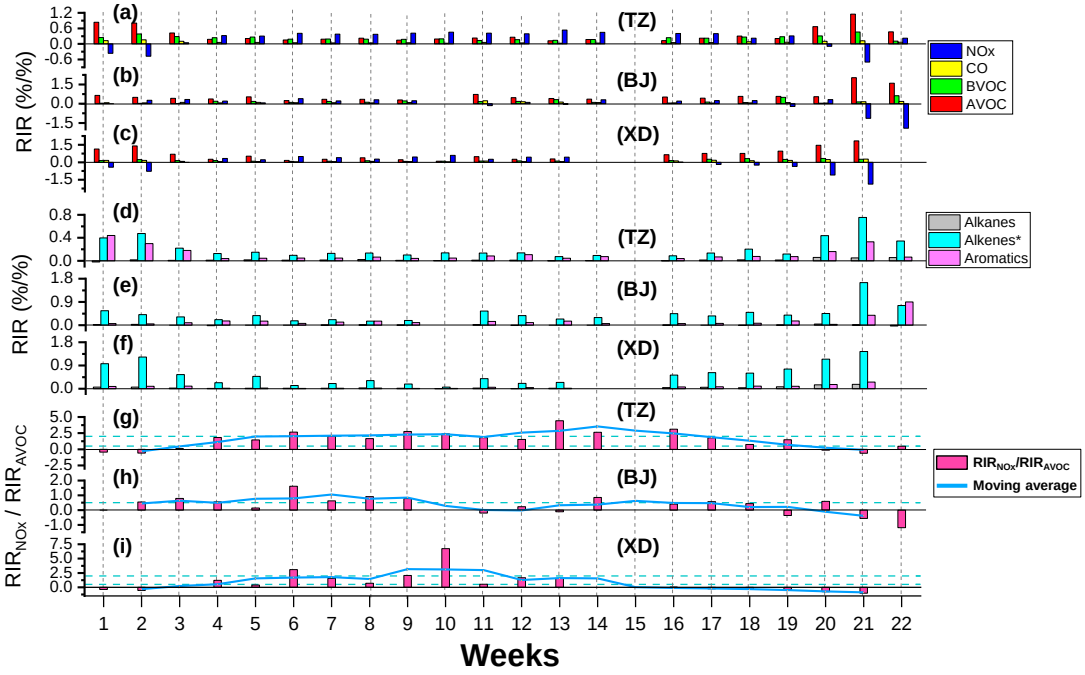

Figure 4. Time series of week-to-week RIR values of major precursor groups and RIR_{NOx}/RIR_{AVOC} at three sites (TZ, BJ, and XD) in Zibo. The blue lines in (g)-(i) are the three points moving average of RIR_{NOx}/RIR_{AVOC} value.

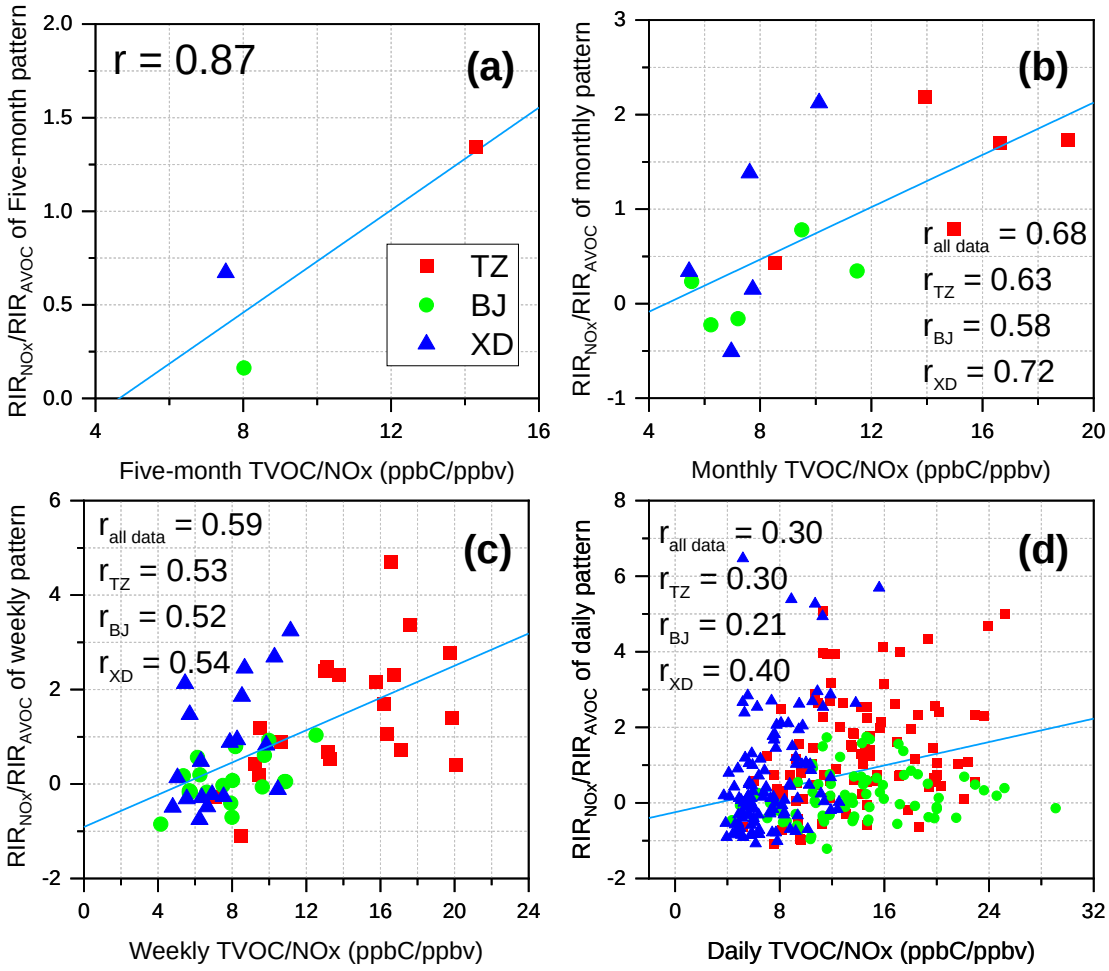

Figure 5. The correlations of TVOC/NO_x with RIR_{NOx}/RIR_{AVOC} at multiple patterns of time scale at the three sites in Zibo.

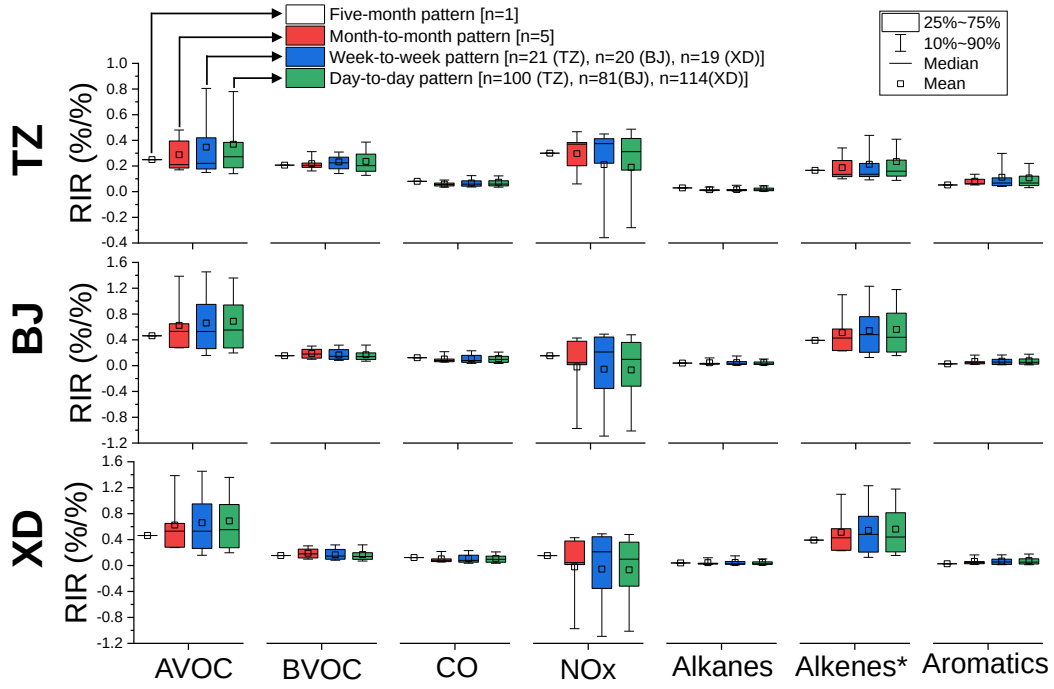

Figure 6. Distribution of RIR values of major precursor groups in multiple patterns of time scale at three sites (TZ, BJ, and XD) in Zibo.

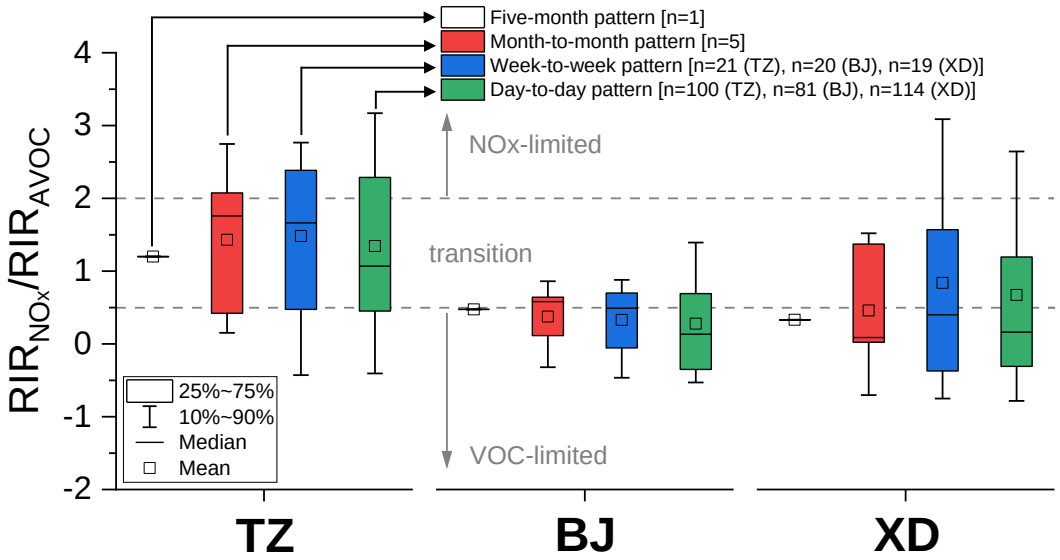

933

934 **Figure 7.** Distribution of RIR_{NOx}/RIR_{AVOC} (indicator of photochemical regime) in multiple patterns of
935 time scale at three sites (TZ, BJ, and XD) in Zibo.

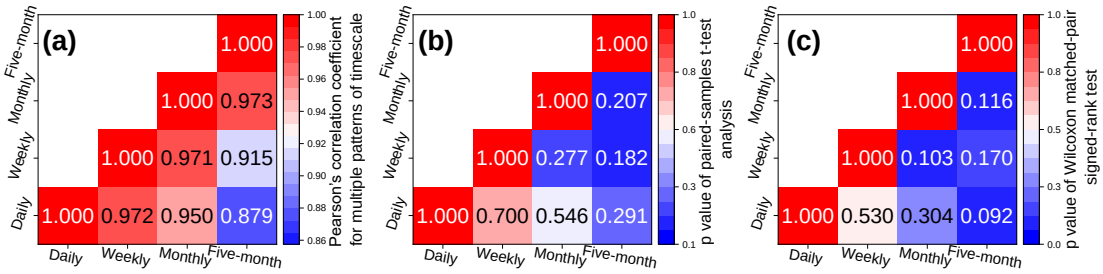

Figure 8. The statistical analysis results of RIR values (from Table S6) at multiple patterns of time scale: (a) Pearson's r correlation analysis (all the results have passed statistical significance assumed at $p <$ 0.01), (b) Paired-samples t-test analysis ($^{*}p$ values refer to differences with a statistical significance assumes at p <0.05), (c) Wilcoxon matched-pair signed-rank test ($^{*}p$ values refer to differences with a statistical significance assumes at p <0.05).

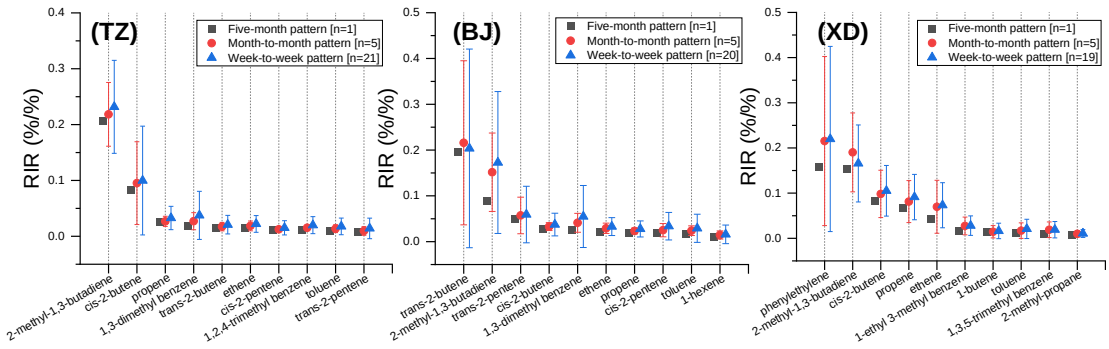

Figure 9. Averaged RIR values of individual AVOC species (top 10) at different patterns of time scale at three sites (TZ, BJ, and XD) in Zibo. The error bars represent the standard deviations of the mean.